Contribution of the wind and Loop Current Eddies to the circulation in the southern Gulf of Mexico

Erick R Olvera-Prado[1], Rosario Romero-Centeno[1], Jorge Zavala-Hidalgo[1], Efrain Moreles[2], and Angel Ruiz-Angulo[3]

[1]Instituto de Ciencias de la Atmósfera y Cambio Climático, Universidad Nacional Autónoma de México
[2]Instituto de Ciencias del Mar y Limnología, Universidad Nacional Autónoma de México
[3]Institute of Earth Sciences, University of Iceland

December 27, 2022

Abstract

The Bay of Campeche in the southern Gulf of Mexico (GoM) is characterized by a semi-permanent cyclonic circulation commonly referred to as the Campeche Gyre (CG). Several studies, documenting its upper layer structure, have suggested a relationship between its seasonal occurrence and the wind, and have proposed that non-seasonal variability arises mainly from interaction of the gyre with Loop Current Eddies that arrive in the region. Other studies have shown that the topography of the region is such that an equivalent-barotropic flow can develop, confining the CG to the west of the bay. Nevertheless, a partition of the contributions of these forcings to the circulation of the gyre in a statistically consistent manner is still needed. In this study, the wind-and eddy-driven circulation are examined with a set of long-term numerical simulations of the GoM using HYCOM. Our results show that, in the absence of eddies, the wind is able to sustain a seasonal-modulated circulation in the CG, confined within the upper 600 m. When LCEs are taken into consideration, the gyre appears to extend below 1000 m, however this behavior results from the presence of the cyclonic bottom boundary current in the southern GoM. Interaction with eddies impose high fluctuations in the circulation of the gyre at intraseasonal time scales, leading to reversals in the current if the event is strong. Additionally , we provide evidence of a northward flux of cyclonic vorticity out of the bay during eddy-gyre interaction events. Finally, we found that the role of topography manifests similarly among these different dynamic conditions, resulting in closed geostrophic contours to the west of the bay that confine an upper-layer, symmetric, equivalent-barotropic CG.

Contribution of the wind and Loop Current Eddies to the circulation in the southern Gulf of Mexico

Erick R. Olvera-Prado[1*], Rosario Romero-Centeno[1], Jorge Zavala-Hidalgo[1], Efrain Moreles[2] and Angel Ruiz-Angulo[3]

[1*]Instituto de Ciencias de la Atmósfera y Cambio Climático, Universidad Nacional Autónoma de México, Mexico City, 04510, Coyoacan, Mexico.

[2]Instituto de Ciencias del Mar y Limnología, Universidad Nacional Autónoma de México, Mexico City, 04510, Coyoacan, Mexico.

[3]Institute of Earth Sciences, University of Iceland, 102 Reykjavik, Iceland.

*Corresponding author(s). E-mail(s): erick@atmosfera.unam.mx; Contributing authors: rosario@atmosfera.unam.mx ; jzavala@atmosfera.unam.mx ; moreles@cmarl.unam.mx ; angel@hi.is;

Abstract

The Bay of Campeche in the southern Gulf of Mexico (GoM) is characterized by a semi-permanent cyclonic circulation commonly referred to as the Campeche Gyre (CG). Several studies, documenting its upper layer structure, have suggested a relationship between its seasonal occurrence and the wind, and have proposed that non-seasonal variability arises mainly from interaction of the gyre with Loop Current Eddies that arrive in the region. Other studies have shown that the topography of the region is such that an equivalent-barotropic flow can develop, confining the CG to the west of the bay. Nevertheless, a partition of the contributions of these forcings to the circulation of the gyre in a statistically consistent manner is still needed. In this study, the wind- and eddy-driven circulation are examined with a set of long-term numerical simulations of the GoM using HYCOM. Our results show that, in the absence of eddies, the wind is able to sustain a seasonal-modulated circulation in the CG, confined within the upper 600 m. When LCEs are taken into consideration, the gyre appears to extend below 1000 m, however this behavior results from the presence of the cyclonic bottom boundary current in the southern GoM. Interaction with eddies impose high fluctuations in the circulation of the gyre at intraseasonal time scales, leading to reversals in the current if the event is strong. Additionally, we provide evidence of a northward flux of cyclonic vorticity out of the bay during eddy-gyre interaction events. Finally, we found that the role of topography manifests similarly among these different dynamic conditions, resulting in closed geostrophic contours to the west of the bay that confine an upper-layer, symmetric, equivalent-barotropic CG.

Keywords: Gulf of Mexico,Campeche Gyre, Seasonal variability, Non-seasonal variability, Topographic control, HYCOM

1 Introduction

The Bay of Campeche (BoC) is a semi-enclosed region located in the southern Gulf of Mexico (GoM), bound to the west, south and east by the coast of Mexico and connected with GoM waters to the north. Its bathymetry follows approximately a U shape with a smooth slope on the western side and a rough slope to the east. The western part of the BoC is characterized by a semi-permanent cyclonic circulation, often referred to as the Campeche gyre (CG) (Monreal-Gómez and Salas de León, 1997), in waters of depths greater than 1000 m; while the circulation on the shelfs presents strong seasonality driven by the wind (Zavala-Hidalgo et al, 2003). Several observational, theoretical and numerical studies have documented the surface and vertical extension of the CG in addition to its seasonal and non-seasonal variability; nevertheless, the contribution of the mechanisms responsible for sustaining the CG is still not fully understood, namely, the wind stress curl (Gutiérrez de Velasco and Winant, 1996; Vázquez de la Cerda et al, 2005; Dimarco et al, 2005), eddy-driven vorticity fluxes (Ohlmann et al, 2001; Vidal et al, 1992), and the confinement effect of the topography (Pérez-Brunius et al, 2013; Zavala Sansón, 2019).

Using a set of observational data, Vázquez de la Cerda et al (2005) presented the first evidence that the observed long-term mean cyclonic circulation within the BoC (in the upper 800 m) could be forced by the positive wind stress curl that prevails in the region (Gutiérrez de Velasco and Winant, 1996) via Sverdrup dynamics, inferring the existence of a western boundary current at 20°N that balances the northward transport within the BoC caused by the wind. From their near-surface drifter analysis, a maximum in the winter and a minimum in the summer in the western boundary current was found, however, the authors considered that the drifter records were not sufficiently long to define the seasonal variability of the mean circulation in a statistically reliable manner. Furthermore, they found that the geostrophic transport estimated from the hydrographic data is in agreement with the Sverdrup transport estimated from the mean wind stress curl (∼4 Sv). Pérez-Brunius et al (2013) found no significant differences in mean currents between winter and summer from high-resolution mooring and drifter data, although the mean values suggest a slight intensification at the western boundary during winter. However, they consider that there is still no conclusive evidence of a western intensified flow in any of the seasons.

On the other hand, some studies suggest that Loop Current Eddies (LCEs) traveling on a southern path (Vukovich, 2007) towards the western boundary and colliding with it influence the CG variability. Ohlmann et al (2001) showed that eddies play a role as important as wind stress in driving the overall GoM circulation on long time scales. Vidal et al (1992) concluded that the collision of a LCE with the southwestern continental shelf led to a transfer of mass and angular momentum towards the south, thus producing a cyclonic gyre in the BoC. In their numerical study, Romanou et al (2004) suggest that the cyclonic circulation in the BoC is caused by accretion of cyclones generated in the western Gulf by interaction of LCEs with the continental slope. From an Empirical Orthogonal Function analysis of eight years of altimetry data, Vázquez de la Vázquez de la Cerda et al (2005) found evidence of a net eddy flux into the BoC which is manifested as smaller-in-size cyclones and anticyclones entering the region, which they hypothesized are generated when LCEs collide with the western continental slope. However, they state that while such eddy flux can explain the non-seasonal character of the circulation, this is simply a supplement superimposed on a larger-scale permanent cyclonic circulation due to the wind stress curl over the BoC. More recently, with the aid of 3 years of surface drifters and altimetry data, Pérez-Brunius et al (2013) analyze three examples of LCEs influencing the CG circulation. The authors found no clear evidence of an influx of positive vorticity into the BoC by cyclones generated by LCE collisions with the western boundary. In fact, in two of the three cases analyzed, they found that the presence of LCEs at the northwestern boundary nearly disrupted the cyclonic gyre rather than intensifying it, draining it of its waters while pushing it towards the southwestern shelf.

Pérez-Brunius et al (2013) addressed the confinement effect of the bathymetry on the CG with three years of current meter moorings. The authors evaluated the vertical coherence of the flow and found that the cyclonic gyre is vertically coherent and nearly unidirectional, consistent with an equivalent-barotropic flow with a reference depth of $H_0 = 650m$. This reference depth results in closed geostrophic contours in the western BoC, explaining, by potential vorticity conservation, the location and the symmetry of the CG west of 94°W. Zavala Sansón (2019)studied the formation of the CG with a nonlinear, time-dependent, equivalent-barotropic model. The author performed idealized wind-driven simulations with decremental values of the reference depth and found that when $H_0 = 650m$, the resemblance of the cyclonic gyre with the CG is high, confirming that the positive circulation over the BoC is compatible with equivalent-barotropic dynamics.

In this study, we address the contribution of the wind and LCEs to the mean, seasonal and intraseasonal variability of the circulation in the western BoC. What distinguishes this study from previous studies is that we use a set of long-term, free-running simulations conducted with an ocean general circulation model with realistic bathymetry and stratification structure, isolating the effects of these processes to discern their relative contributions. First, the separate and joint mean effect of wind and LCEs on the extent and vertical structure of the CG is examined, providing insight about the role of topography under these different dynamic conditions. Then the role of the wind stress curl in modulating the seasonal variability of the CG in the presence and absence of LCEs is explored. Finally, we discuss the non-seasonal variability of the CG induced by LCEs entering the northern BoC and examine the associated vorticity flux. Our results may provide more insight on the long-term effect of these forcings on the circulation of the BoC in a statistically consistent manner, and thus advance in the understanding of the dynamics of the region. The model configuration, validation and analysis methods used are described in Section 2; results and discussion, including the analysis of the mean state and vertical structure of the CG, are presented in section 3. In this section, the vorticity flux through the BoC induced by LCEs is also examined. A brief concluding summary is provided in section 4.

2 Model and methods

2.1 The numerical simulations

To address the contribution of the different processes to the circulation in the BoC, three free-running simulations of the GoM with incremental complexity and realism were conducted employing HYCOM. HYCOM uses a generalized hybrid vertical coordinate system that allows vertical coordinates to follow isopycnal layers in the deep stratified ocean and transition to pressure coordinates or terrain-following coordinates in unstratified regions or coastal areas, respectively (Bleck, 2002; Chassignet et al, 2006). The horizontal domain covers the GoM, the northwestern Caribbean Sea, and part of the western North Atlantic Ocean ([98°W, 77°W] x (18°N, 32°N]), with a spatial resolution of 1/25° (∼3.8-4.2 km) and 36 hybrid vertical layers, which are mainly isopycnal layers in the open ocean below the mixed layer and z-layers above it. The model bathymetry is an integration from different sources: the one from the HYCOM website (hycom.org), the General Bathymetric Chart of the Oceans (GEBCO), and corrected data from different sources, mainly observations collected during several cruises. Monthly climatology of river inflow is simulated at 40 locations along the coast and no data assimilation nor tidal forcing was used. More details of the model parameters for the three experiments are listed in Table 3.

The three simulations share the specifications mentioned above. Experiment OBW (Open Boundaries with Wind) is the control run since it is the most realistic simulation; in experiment NoOBW (No Open Boundaries with

Wind), the lateral boundaries are closed to remove the Loop Current system and thus the influence of LCEs, and focus on the isolated effect of wind over the BoC; and in experiment OBNoW (Open Boundaries without Wind), the atmospheric forcing is turned off in order to discern the influence of LCEs in the absence of wind forcing. OBW is initialized from the mean state of January, 1994 of the 1/12° GOFS 3.1 HYCOM global reanalysis (GLBb0.08-53.X) (Metzger et al, 2017), reaching statistical stability within a few months, as shown in the time series of global mean Kinetic Energy averaged over the 3D domain (fig. 3g red line). Then, NoOBW and OBNoW were initialized from a 1-year spin-up of the OBW output (January 1st, 1995). After statistical stability is reached in these experiments (fig. 3g blue and green lines), they were integrated from 1997-2015, which encompasses the analysis period for this study.

OBW and OBNoW were nested in the global reanalysis using monthly boundary conditions from a 22-year climatology (1994–2015). This monthly climatology is repeated each year to produce the continuous 19-year model integration, therefore, no interannual variability is imposed at the lateral open boundaries. Following spin-up, hourly atmospheric forcing (10-m wind speed, 2-m air temperature, 2-m atmospheric humidity, surface shortwave and long-wave heat fluxes, surface atmospheric pressure, and precipitation) is prescribed for OBW and NoOBW using the Climate Forecast System Reanalysis (CFSR) (Saha et al, 2010) from 1997-2015. Wind stress is calculated using bulk formulas during model run time taking into account the current speed. The target densities, which define the vertical grid in the model, are inherited from the global reanalysis. The outputs of the model, which include the estimated wind stress fields, were recorded every day.

2.2 Validation of the model

Since the simulations are not constrained by data assimilation and owing to the lack of realism in the variability of the boundary conditions, GoM transitory features like LCEs do not necessarily match observations at a specific time. Therefore, evaluation of the model performance consisted in verifying that the major characteristics of the GoM circulation were in statistical agreement to those obtained based on observations; this provides confidence that the CG and its response to the LCEs and wind forcings are realistic. The validation is carried out on the OBW experiment (control). Here, we compare statistical analysis derived from simulated velocity and sea surface height (SSH) with analysis of in-situ and remote sensing observations. Some of the diagnostics presented here, follow the methodology used in Morey et al (2020). In general, the simulation is able to reproduce the more energetic patterns and the intrinsic variability of the GoM, including its amplitude, location and evolution.

Table 1 Specifications of the numerical simulations using the HYCOM model. OBW is the control run, NoOBW corresponds to the experiment with closed boundary conditions, and OBNoW corresponds to the experiment without atmospheric forcing.

Experiment	**OBW (Control)**	**NoOBW**	**OBNoW**
Hycom version	2.3.01	2.3.01	2.3.01
Lateral boundaries	Monthly climatology	No	Monthly climatology
Atmospheric forcing	Hourly (CFSR)	Hourly (CFSR)	No
Vertical coordinates	36 hybrid layers	36 hybrid layers	36 hybrid layers
Initialization	(1-Jan-1997)	Hotstart (1-Jan-1997)	Hotstart (1-Jan-1997)
Length (years)	19	19	19
Baroclinic time step	120 s	120 s	120 s
Barotropic time step	7.5 s	7.5 s	7.5 s
Reference density (σ)	34	34	34
Vertical turbulence	KPP	None	KPP
Sea Surface Salinity nudging	Generalized Digital and Environmental Model–V4.0 and (GDEM4)		
Quadratic bottom drag coefficient	Spatially varying (min = $2.49x10^{-3}$, max = $7.54x10^{-3}$)		
Velocity diffusion (veldf2) [m/s]	Spatially varying (min = $2.36x10^{-3}$, max = $2.65x10^{-3}$)		
Horizontal viscosity	Max[background Laplacian (veldf2), Smagorinsky] + biharmonic (0.02 m/s)		

2.2.1 Mean circulation and transport

Figure 1a shows the standard deviation of SSH from the OBW experiment and figure 1b that computed with the Copernicus Marine Environment Monitoring Service (CMEMS) database (https://doi.org/10.48670/moi-00148). CMEMS consists of daily instantaneous maps of SSH anomalies in a 0.25°x0.25° grid and covers the period from January 1st, 1993 to December 31st, 2020. The model produces a relatively realistic variability, with a primary area of high values within the LC extension and retraction region and a secondary area highlighting the preferred paths of the LCEs and the otherwise known LCE graveyard, while CMEMS depicts smaller values in the western GoM. In the BoC, small standard deviation values are found in both datasets, indicating persistence of the flow. The structure of the mean along-channel velocity through the Yucatan Channel and the Florida Straits for the 19 years of simulation is shown in figure 1c and from observations in figure 1d. Observations come from in situ moorings deployed during the CANEK project (Candela et al, 2019) and cover the period from July 2012 to July 2018 . In general the model is consistent with observations, the Yucatan main current, counter-current and undercurrent are overall well represented, with the core of the main current placed at $\sim 86.3W$. The core of the current in the Florida Straits is weaker and depicts a northern displacement in the model compared to observations. The modeled Yucatan Channel climatological transport shows strong seasonality (Fig. 1e), with a mean of about 28 Sv, which is within the range of published estimates ranging from 23.8 to 30.3 Sv (Athié et al, 2015; Rousset and Beal, 2010; Sheinbaum et al, 2002). The model exhibits moderate interannual variability in the transport, which is to be expected given that there is no interannual variability at the open boundaries. Observed climatological transport (Fig.

1f) is derived from 59-month mooring data (Athie et al, 2020) and depicts a maximum increase in July of 31.4 Sv and a minimum of 24.9 Sv in March.

The mean deep circulation between 1500-2500 m was computed for the three experiments throughout the 19 years of simulation in order to verify or discard the presence of the large-scale circulation patterns found in observational data (Fig. 1j) (Pérez-Brunius et al, 2018; Furey et al, 2018) and other numerical studies (Morey et al, 2020; Olvera-Prado et al, 2022). In general, OBW and OBNoW (Figs. 1g and 1i) are able to reproduce the cyclonic current around the boundary of the basin, the cyclonic Sigsbee Abyssal Gyre and the cyclone-anticyclone dipole and the cyclonic circulation to the south of it, below the LC. There are, however, some significant differences in the magnitude of mean velocity between both experiments associated with the three major circulation features mentioned above, in which OBW depicts stronger velocities overall. On the other hand, the only circulation pattern present in NoOBW (Figure 1h) is a weak Sigsbee Abyssal Gyre that is smaller in size. These results confirm that open boundary conditions, and therefore the presence of the LC system, in OBW and OBNoW are responsible for the presence of these deep patterns, at least partially, and suggest that wind along with potential vorticity conservation are capable of inducing a weak cyclonic circulation in the Sigsbee abyssal plain.

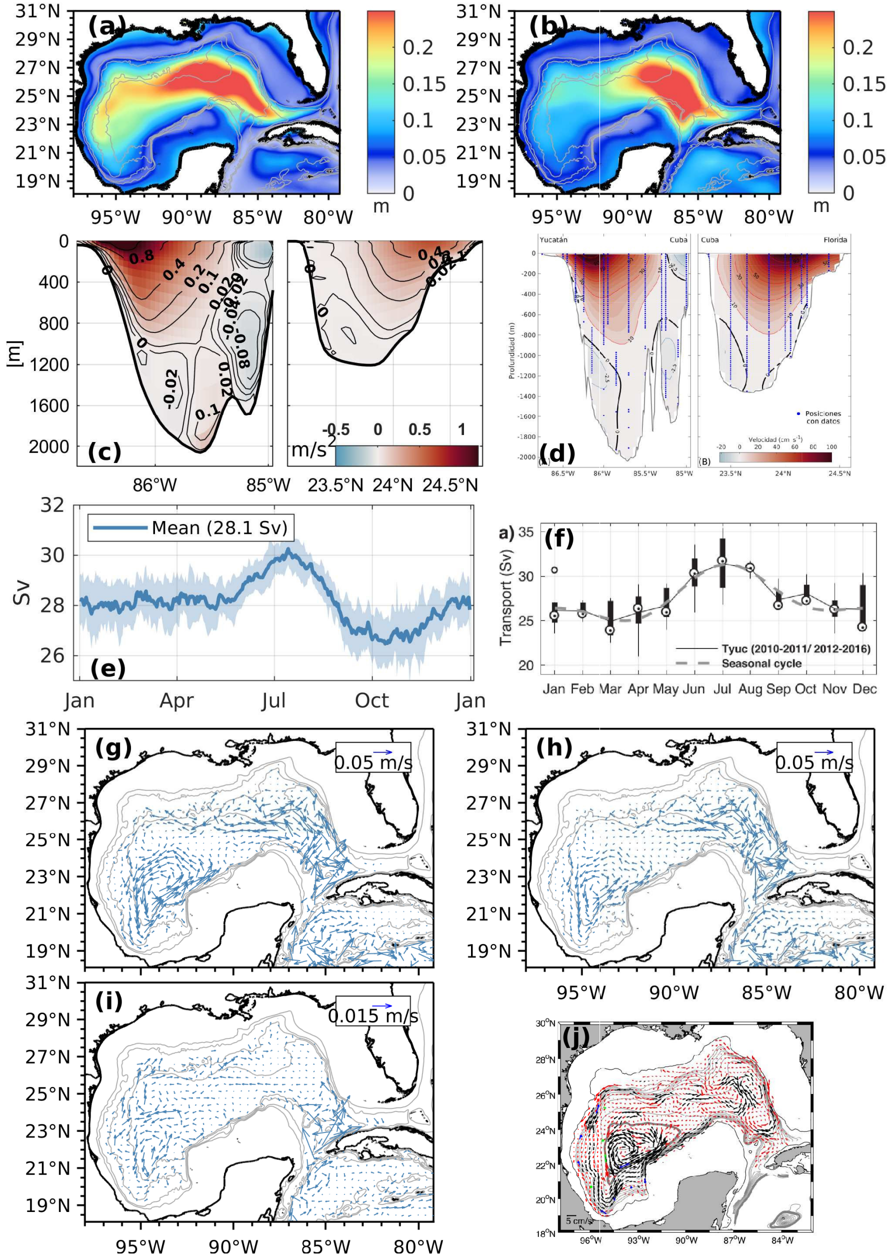

Fig. 1 Model validation: Standard deviation of the SSH from (a) OBW and (b) CMEMS (https://doi.org/10.48670/moi-00148); mean along-channel velocity component in the Yucatan Channel and Florida Straits from (c) OBW and (d) mooring data (from Candela et al (2019)); climatological transport through the Yucatan Channel from (e) OBW and (f) mooring data (from Athie et al (2020)); and mean deep circulation between 1500-2500 m for experiments (g) OBW, (h) OBNoW, (i) NoOBW and from (j) observations (from Pérez-Brunius et al (2018)).

2.2.2 LC and LCE metrics

Following Dukhovskoy et al (2015), the LC and LCEs are tracked using the 0.17-m contour in demeaned SSH fields. These are calculated by subtracting the spatial mean from each SSH field record, in order to remove bias in the surface elevation fields associated with seasonal height variations due to upper-ocean warming and cooling. Then, the detachment of a LCE from the LC is defined to occur when the 0.17-m contour "breaks", resulting in two separate contours, in which the first defines the LC and the second the detached LCE. We only consider events when eddies detach and ultimately dissipate, which are commonly known as separation events. The date of each LCE separation event is the date that the 0.17-m LC tracking contour breaks (Leben, 2005; Dukhovskoy et al, 2015). From the objective tracking technique applied to the 19-year record of SSH, a total of 34 separation events were identified, yielding a mean LCE separation period of 6.8 months. The main characteristics of the 34 LCEs are listed in table 2. The propagation trajectories of the 34 LCEs are shown in figure 2a, which show good agreement with observations (Fig. 2b) (Donohue et al, 2008). The normalized histograms of the distribution of LCE separation events and number of separation events by month from the model are shown in figure 2c and d respectively (blue bars) along with the corresponding histogram from the CMEMS database (red lines). In general, there is good-agreement between the distribution of the LCE separation period derived from the model and from observations, both depicting asymmetric, positively skewed distribution of the data. The mean LCE separation period from observations is 7.1 months. The seasonal distribution of separation events from the model and observations show two relative peaks, one in winter/spring and another in summer.

LC metric statistics based on the tracking of the 0.17-m SSH contour were derived from the 19-year simulation data and the 28-year CMEMS SSH dataset, to be directly compared between them. The normalized histograms of the LC northernmost latitude reveal unimodal distributions in both cases, with the peak centered on the 27.4-27.6°N bin and a mean on 26.9°N for the model (Fig. 2e), and the peak centered on the 26.8-27°N bin and a mean on 26.4°N for the observations (Fig. 2f). The distribution of the LC area in the model and altimeter-derived data also depicts unimodal distributions, with the mode centered on 180,000-190,000 km2 and the mean on 163,021 km^2 for the model (Fig. 2g), and the mode centered on 140,000-150,000 km^2 and the mean on 137,235 km^2 for the observations (Fig. 2h).

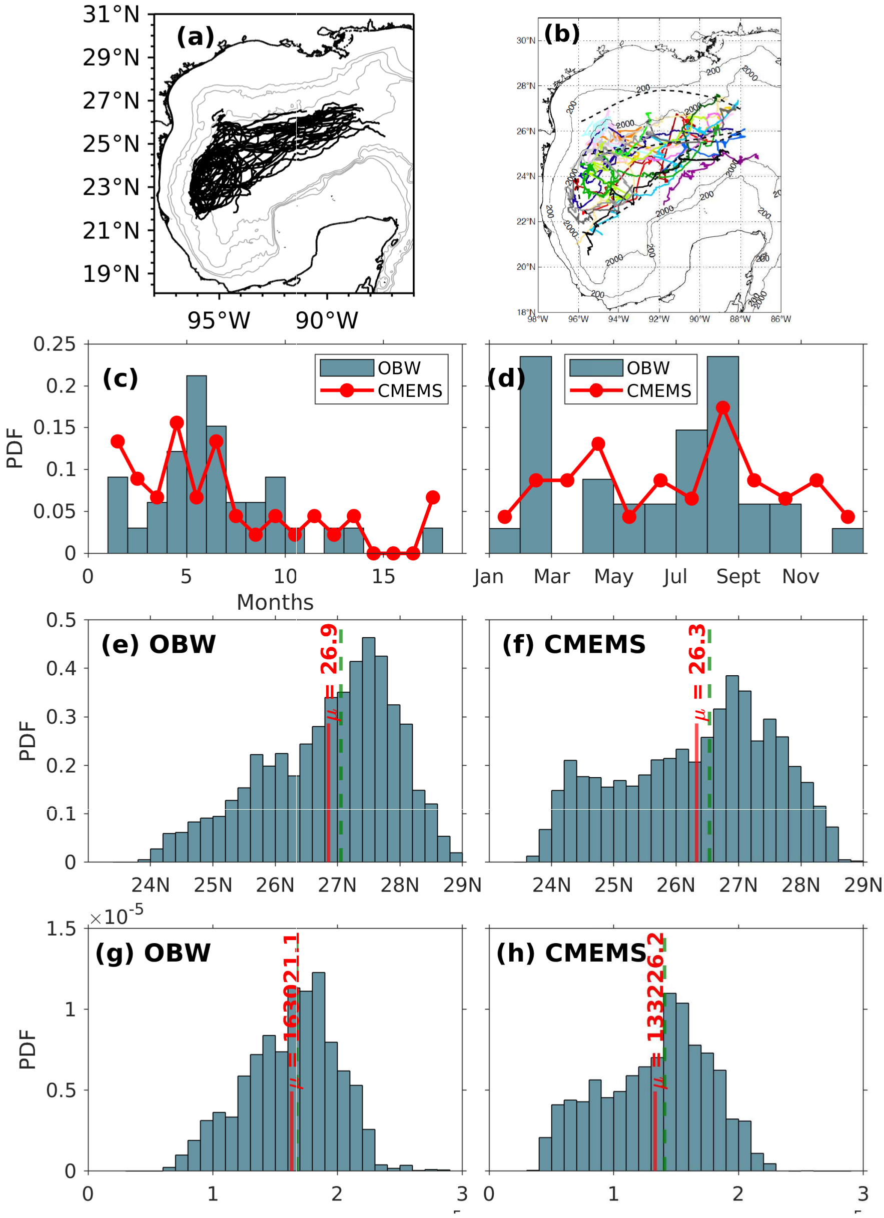

Fig. 2 (a) Trajectories of every LCE from HYCOM, (b) trajectories of every LCE from observations (from Donohue et al (2008)), comparison of normalized histograms of (c) LCE separation period and (d) monthly occurrence between the model and the CMEMS database, comparison of normalized histograms of LC northernmost latitude between (e) the model and (f) CMEMS, and comparison of normalized histograms of LC area (x$10^5 km^2$) between (g) the model and (h) CMEMS

Table 2 Characteristics of the LCE separation events from the OBW experiment: 1 January 1997 through 31 December 2015.

LCE number	Separation date	Separation period (months)	Lifespan (days)	Reached BoC	Area (km^2)
1	28 Aug 1997	15.03	385	Yes	68,345
2	20 May 1998	8.72	345	Yes	62,309
3	7 Oct 1998	4.61	325	No	22,877
4	19 Jul 1999	9.37	249	No	38,591
5	26 Oct 1999	3.26	323	Yes	34,181
6	26 May 2000	7.2	154	No	28,849
7	21 Jul 2000	1.84	377	Yes	94,699
8	22 Feb 2001	7.11	288	Yes	32,760
9	18 Aug 2001	5.82	367	Yes	55,429
10	27 Feb 2002	6.35	285	Yes	46,921
11	30 Aug 2002	6.05	254	No	37,098
12	26 Feb 2003	5.92	315	Yes	48,936
13	17 Aug 2003	5.66	394	Yes	72,537
14	7 Apr 2004	7.7	268	No	44,799
15	23 Feb 2005	10.59	295	Yes	64,517
16	19 Aug 2005	5.82	355	Yes	67,259
17	5 Feb 2006	5.59	392	No	33,606
18	12 Jul 2007	17.17	426	No	57,246
19	18 Apr 2008	9.24	144	No	15,430
20	30 Jul 2008	3.39	42	No	31,220
21	22 Sep 2008	1.78	360	No	25,674
22	29 Jun 2009	9.21	167	Yes	25,315
23	30 Aug 2009	2.04	370	Yes	69,733
24	13 Jan 2010	4.47	293	No	58,767
25	14 Feb 2011	13.06	250	No	59,025
26	29 Jul 2011	5.43	392	No	39,776
27	16 Feb 2012	6.64	853	No	44,789
28	17 Jun 2012	4.01	300	Yes	50,593
29	24 Dec 2012	6.25	327	Yes	55,370
30	13 Feb 2013	1.68	276	No	43,056
31	8 Aug 2013	5.79	341	Yes	49,421
32	11 Aug 2014	12.11	321	Yes	75,697
33	22 Apr 2015	8.35	254	No	61,020
34	3 Sep 2015	4.41	119	No	40,506

2.2.3 Kinetic Energy of the deep flow

The eddy kinetic energy per unit mass (EKE) and the kinetic energy per unit mass of the mean flow (MKE) from the model velocity time series (u,v) at each model grid point, between 1500-2500 m, were analyzed and compared with the corresponding quantities derived from the binned float velocities by Pérez-Brunius et al (2018) and presented in Morey et al (2020). EKE is computed as:

$$EKE = \frac{1}{N}\sum_{i=1}^{N}\frac{\left[(u_i-\bar{u})^2+(v_i-\bar{v})^2\right]}{2} \tag{1}$$

and MKE is computed as:

$$MKE = (\bar{u})^2 + \bar{v})^2)/2 \tag{2}$$

where $(\bar{u}, \bar{v})$ are the mean velocity vectors and N the length of the time series. In general, the model simulates weaker variability of the velocity in the deep layer of the GoM, as quantified by the EKE (Fig. 3a), than observed by the floats (Fig. 3b). Both datasets depict enhanced EKE in the eastern part of the basin compared to the western part, but with the EKE of the binned float velocities showing higher magnitude and covering and covering a wider region. Inspection of the MKE fields shows that in the Sigsbee Abyssal Gyre the model (Fig. 3c) presents similar magnitude to that computed from the float trajectories (Fig. 3d), but in the model this feature extends southward and westward towards the Bay of Campeche including which appears to be the bottom boundary current, whereas the observations show a distinct separation between both features. Also, the model shows a region of high MKE along the northwestern Campeche Bank in agreement with observations.

Finally, as in Pérez-Brunius et al (2018), the ratio of MKE to the total kinetic energy, MKE/(MKE + EKE) is computed in the model data as an indicator of the relative persistence of the mean circulation (Fig. 3e), and compared to the corresponding ration derived from the binned float velocities (Fig. 3f). In general both datasets show similar behavior and magnitude, the Sigsbee Abyssal Gyre is highlighted by larger values of this quantity due to its relative persistence. Low values in the eastern GoM are also present, suggesting that the eddy structure under the LC region, namely, the anticyclone-cyclone dipole and the cyclone to the south of it are highly variable. The cyclonic boundary current also appears to be a transient feature around most of the basin evident only in the long-term mean.

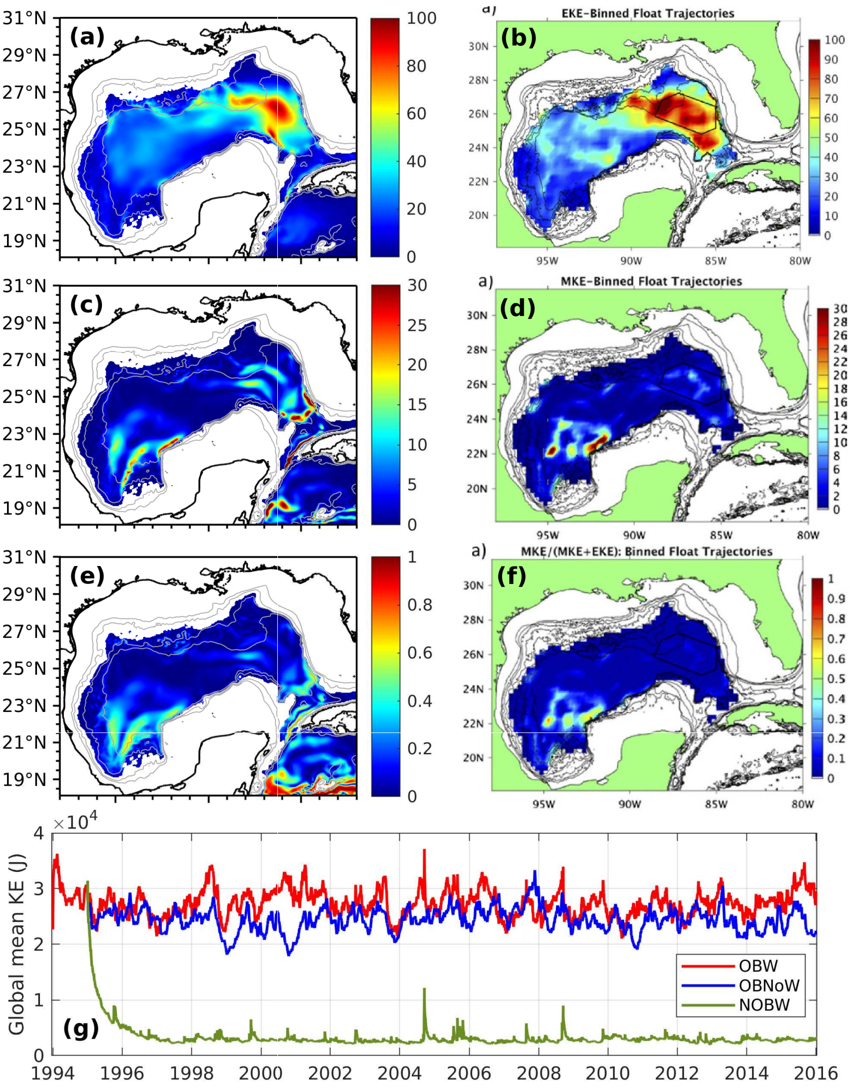

Fig. 3 EKE (cm^2 s^{-2}) derived from (a) the model (OBW) and (b) the observed float velocities (from Morey et al (2020)), MKE (cm^2 s^{-2}) derived from (c) the model (OBW) and (d) the observed velocities (from Morey et al (2020)), the ratio of MKE to the total kinetic energy per unit mass [MKE/(MKE 1 EKE)]) derived from (e) the model (OBW) and (f) the observed velocities (from Morey et al (2020)), and the time evolution of the global kinetic energy in the model domain (J) from experiments OBW (red line), OBNoW (blue line) and NoOBW (green line).

3 Results

3.1 Mean circulation and vertical structure

We first address the problem of quantifying the mean contribution of the wind and LCEs by examining the mean velocity fields obtained through the 19 years of simulation. Figure 4 shows the mean surface velocity vectors and SSH over the whole domain, and a zoom over the BoC showing velocity vectors and speed contours for the three experiments. Among the main features that can be observed are the following: experiment OBW (Fig. 4a) depicts the Loop Current at an "intermediate" stage over the eastern GoM, and a broad anticyclonic circulation over the central- and north-western regions, commonly referred to as the Western Anticyclonic Gyre, located from 88°W to the west and from ∼22°N to the north of the domain, represented by small negative anomalies after demeaning. To the west of the BoC, the CG is shown centered at around 95.5°W, 20.25°N and is represented by a low dynamic height. The mean circulation in NoOBW, the experiment without lateral boundary forcing, shows the wide anticyclonic circulation in the western GoM as well as the CG in the BoC, although slightly centered to the south compared to OBW. Moreover, since there is no eddy-driven circulation in this experiment, circulation on the shelfs is more evident. On the other hand, OBNoW, the experiment without atmospheric forcing, shows a narrower area of high pressure on average which extends from the LC through the central-western region, which mimics the south-west mean trajectory of LCEs (Vukovich, 2007). However, unlike OBW and NoOBW, OBNoW does not present any signal of a cyclonic circulation in the BoC, at least not on the surface, which suggests the strong dependence of the CG on the wind forcing. Zoom in the BoC shows strong mean speed values in the western and eastern arms of the CG for OBW and NoOBW (Figs. 4 b and d), however, high speed values are also found to the north of the BoC in OBW, which is related to the average presence of LCEs in the western GoM. As a consequence of this, the CG in OBW appears to be flattened by them, compared to NoOBW, in which the CG is less disrupted from its unperturbed state and therefore with a stretched-out shape.

In order to examine its vertical structure, a zonal section through the CG was defined at 20.2°N and between 96.7°W and 94.0°W (red line Fig. 4b) as representative of its center. The mean meridional velocity in the section is shown in figures 5 (a-c) for the three experiments. It is observed that for OBW and NoOBW velocities are surface-intensified (∼0.2 m/s), but for OBW the magnitude decreases steadily up to ∼1000 m, while for NoOBW the gyre seems to be confined within the upper ∼600 m. In both experiments the center of the gyre is located around 95.3°W, and the CG depicts a symmetric shape with similar speed magnitude in the western and eastern arms. Additionally, a revealing characteristic is that in OBW the signal of a cyclonic circulation extends below 1000 m with weaker but steady velocities (∼5 cm/s) throughout the water column to the bottom of the basin.

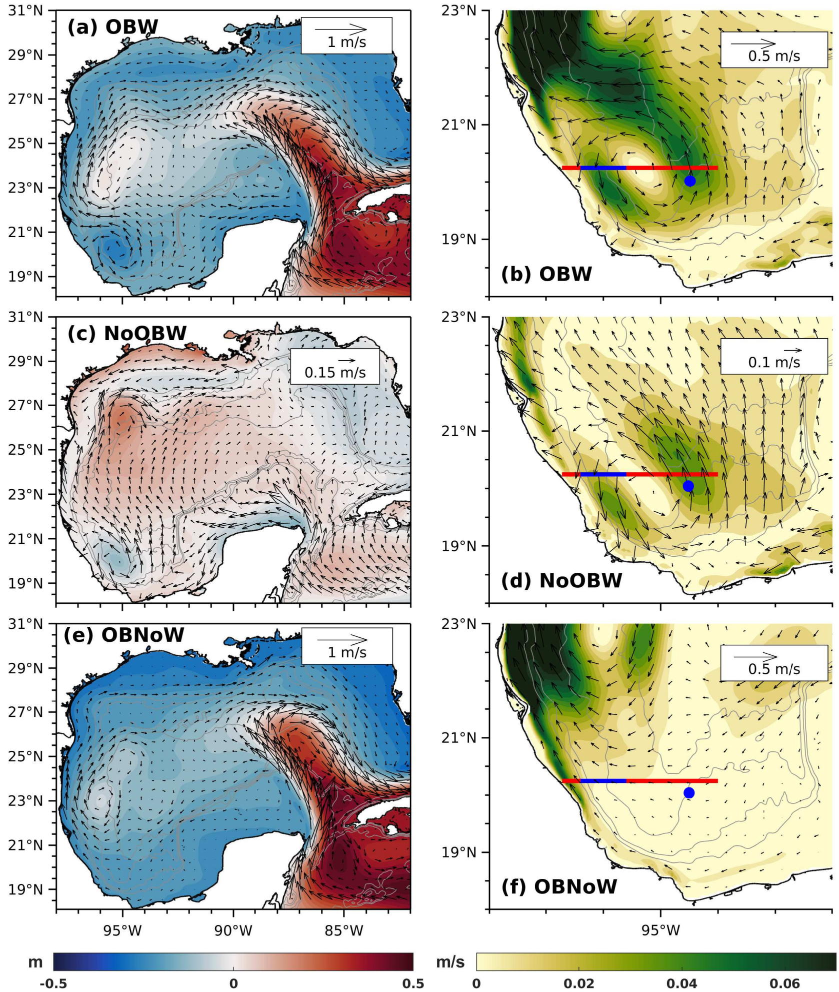

Fig. 4 (a, c, and e) Mean surface velocity vectors and SSH contours for the three experiments in the model domain; and (b, d, and f) surface velocity vectors and speed contours zoomed in the BoC, the red line indicates the zonal section where statistics of the meridional velocity were calculated, the blue line is the zonal section where the transport was calculated and the blue dots show the locations where the vertical coherence of the currents were estimated. The gray contours indicate the 500, 1000, 2000, and 3000 m isobaths.

On the other hand, in OBNoW, the experiment in which wind forcing is turned off and the BoC is only influenced by LCEs, the mean velocity section (Fig. 5c) depicts a weaker, yet symmetric, cyclonic circulation above 1000 m compared to OBW and NoOBW, but below this depth the cyclonic circulation is present as in OBW. The fact that the structure and magnitude of the mean cyclonic circulation below 1000 m in these two experiments are very similar, suggests that this feature is the expression of a separate circulation feature intrinsically related to the LC system. One such candidate is the cyclonic boundary current flowing around most of the deep perimeter of the GoM, reportedly to be located between the 2000- and 3000-m isobaths in observational (Pérez-Brunius et al, 2018) and numerical studies (Morey et al, 2020). Such studies suggest that this deep current is episodic in character, with long periods of cyclonic flow and shorter periods of back-and-forth motion associated with a dominant time scale of ∼14 months, whose variability within the BoC could be related to the coupling of the upper and lower layers of the GoM when a LCE travels westward (Furey et al, 2018; Olvera-Prado et al, 2022). We have shown that such deep feature is indeed present in both experiments, furthermore, the standard deviation of the flow for both experiments (Fig. 5 d and f) shows small variability in the cores of the cyclonic circulation between ∼1500-3000 m which can be associated with the persistence of the current and the findings mentioned above.

The vertical spatial structure of the CG flow variability in the three experiments is well explained by the first two Empirical Orthogonal Function (EOF) modes (Fig. 5 g-l). The first mode depicts a dipole pattern with negative and positive signs in the western and eastern cores respectively in the three cases, similar to the mean velocity pattern, explaining between $\sim 35 - 57\%$ of the variance. This mode seems to describe the intensification and weakening of the CG in the upper ∼1000 m resulting from the variability imposed by the wind (NoOBW), the LCEs (OBNoW), or both (OBW). In fact, variability in the first mode is stronger in experiments OBW and OBNoW, where the BoC is influenced by LCEs, as shown by the high values (> 0.1 m/s) in both sides of the gyre near the surface. Figure 9 (upper panels) shows the principal components of the first mode along with the time series of total transport through the western boundary current in the CG (Section 3.3) throughout the 19-year of each simulation. It can be observed the high relationship between both time series, especially in events of LCE penetration into the BoC (OBW fig. 9 a), the correlation coefficient between the transport and the principal components is ∼0.8 in all the experiments. The second mode, explaining between $\sim 20 - 30\%$ of the variance, displays a tripole pattern in the three cases with the center core probably related with the longitudinal displacement of the center of the CG. The above is in general agreement with the findings of Pérez-Brunius et al (2013), in which the variability of the surface currents in the western basin is mostly due to changes in the size, form, position and intensity of the CG due to its interaction with LCEs.

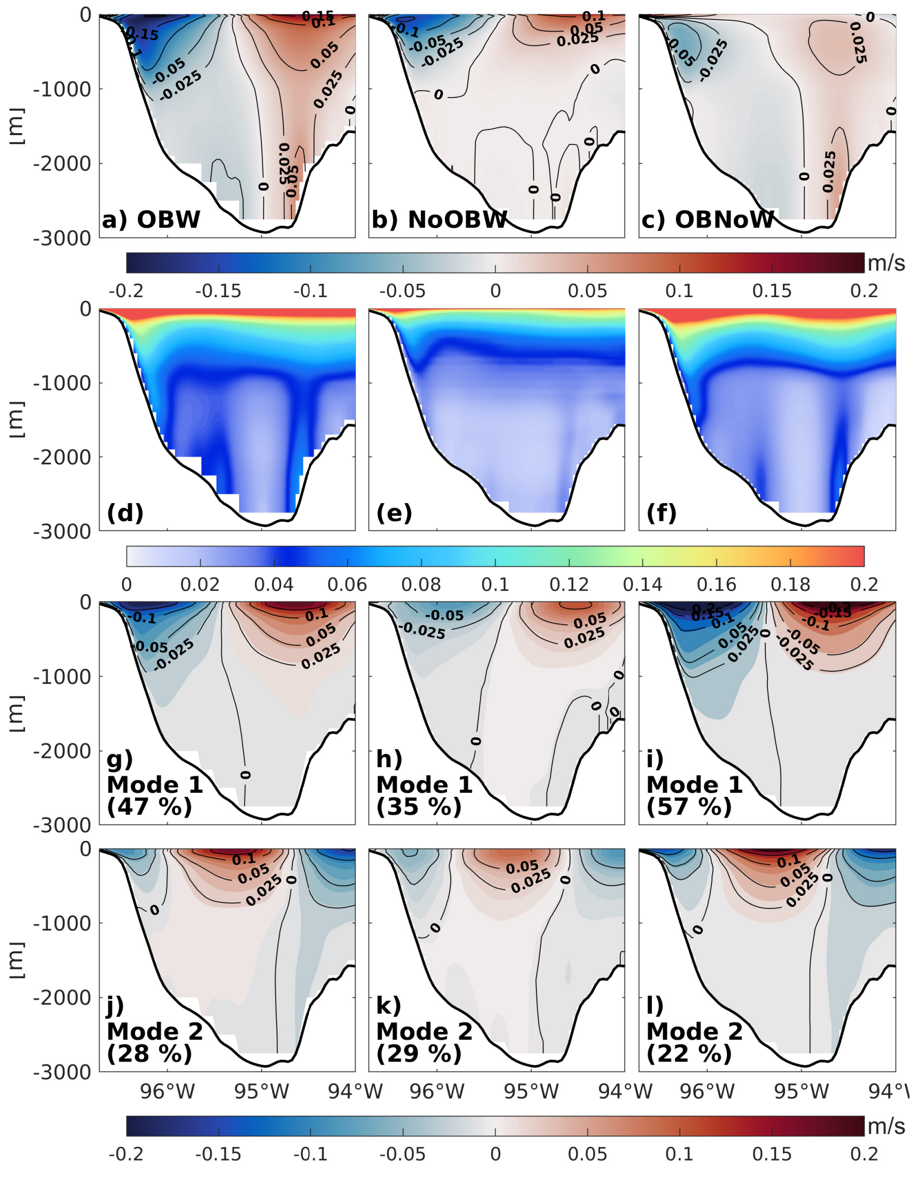

Fig. 5 Mean (a-c) and standard deviation (d-f) of meridional velocity (positive northward) in the CG (at 20.2°N) for the three experiments. First (g-i) and second (j-l) EOF modes of the meridional velocity for the three experiments. In general, EOF-1 explains $\sim 35-57\%$ of the variance and EOF-2 $\sim 20-30\%$ in the three cases.

3.1.1 The role of topography under different dynamic conditions

Our results for the three simulations show that, on average, a symmetric cyclonic gyre is present in the deep western BoC, although with some differences in the vertical extension and strength among these experiments (Figs. 5 a-c). Furthermore, the EOFs analysis applied to the vertical structure of the CG shows that the major mode of variability is consistent with a dipole pattern similar to the mean state but confined to the upper 1000 m (Figs. 5 g-i), suggesting that the principal variability of the CG is controlled by a common factor present the three cases. The implications of this facts are relevant, previous studies indicate that the topography of the basin is such that the flow can be modeled as equivalent barotropic (Pérez-Brunius et al, 2013; Zavala Sansón, 2019), following potential vorticity contours f/F_0, where f is the Coriolis parameter, $F_0 = H_0(1 - e^{-H/H_0})$, H_0 is the equivalent depth, and H the total depth, which happen to be closed in the basin. The authors state that, by conservation of potential vorticity, any flow can exist along those contours in the absence of forcing and dissipation. Furthermore, in the presence of realistic wind forcing this flow can be stronger and present seasonal variability. Our findings reveal that in the absence of wind, the western BoC is capable of developing a net cyclonic circulation in the upper layers under the influence of LCEs (exp. OBNoW fig. 5c), thus corroborating the importance of the topography in organizing upper layer flows.

We explore the role of topography under these different dynamic conditions by evaluating the vertical coherence of the flow in the three cases. We adopted an approach similar to Pérez-Brunius et al (2013) and used two different methods to estimate the equivalent depth from the velocity profile in the model in the eastern flank of the CG (blue dots in figs. 4b, d and f) closest to their CTZ mooring (their fig. 3b), as we consider it the more appropriate location for the evaluation since it is not directly influenced by the continental slope. First, the complex correlation coefficients between the mean model velocity at 40 m and the velocities at deeper depths were computed. Figures 6 a, d and g show the vertical profile of mean horizontal currents for OBW, NoOBW and OBNoW respectively. Then, the depth at which the complex correlation coefficient exceeds 90% is recorded, which is used as a proxy at which velocities are still correlated with the currents at 40 m. It was found that for OBW and OBNoW, the flow is approximately unidirectional from the surface up to 820 and 920 m respectively. In both cases, below this depth the flow rotates clockwise to the east which seems to be the expression of the bottom boundary current. For NoOBW, the coherent upper layer thickness is about ∼450 m, which is shallower than the other two cases.

For the second method, EOFs of the velocity profile, including their mean, were estimated to obtain the first mode of vertical variability. Figures 6 b, e and h show the eigenvector for the first EFO mode for the three experiments, in all the cases the first mode explains $> 80\%$ of the total variance. It can be seen that the vertical coherence of the flow is uniform among the three cases, they all depict unidirectional velocities from the surface up to ∼800-1000 m. After adjusting the function $v(z) = v(0)e^{(z/H_0)}$ to the first modes of vertical variability, we obtain an e-folding scale of H0 ∼950, 900 and 850 m for OBW, OBNoW and NoOBW respectively. See table 3 for the results of the evaluation of the vertical coherence of the flow using both methods. Finally, we plotted the geostrophic contours (f/H_0) for the resulting equivalent depths using the EOF method and found that in the three cases the contours closed in the western BoC (Figs. 6 c, f and i).

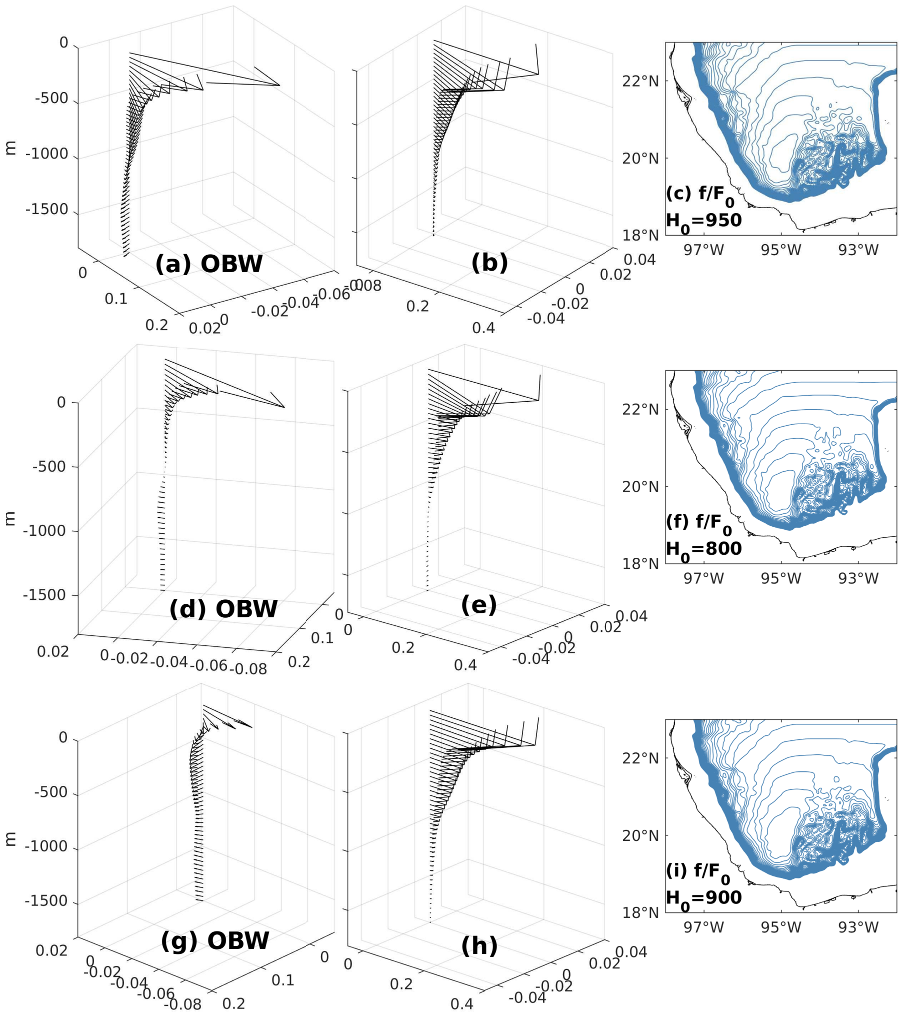

Fig. 6 Vertical profiles of mean horizontal currents and first modes of vertical variability for experiments (a-b) OBW, (d-e) NoOBW and (g-h) OBNoW respectively. Also shown are the geostrophic contours f/F_0 ([4:0.1:10] x$10^{-8}m^{-1}/s^{-1}$) with f the local Coriolis parameter, $F_0 = H_0(1 - e^{-H/H_0})$, H the bottom depth and equivalent depths of (c) $H_0 = 950$ m for OBW, (f) $H_0 = 800$ for NoOBW, and (i) $H_0 = 900$ for OBNoW.

Table 3 Results of the evaluation of vertical coherence of the flow derived from a velocity profile in the model close to the CTZ mooring in Pérez-Brunius et al (2013). First row shows the complex correlation coefficient between the mean currents at 40 m and the currents at different depths, in particular the maximum depth for which R >= 0.90. Second row shows the equivalent depth H_0 after adjusting the function $v(z) = v(0)e^{(z/H_0)}$ to the first modes of vertical variability.

Method/experiment	OBW	NoOBW	OBNoW
Mean velocity (m)	820	450	920
EOF (m)	950	800	900

3.2 Seasonal modulation of the Campeche Gyre

The seasonal modulation of the CG has been addressed by several authors from different perspectives (Pérez-Brunius et al, 2013; Vázquez de la Cerda et al, 2005). The current consensus is that the wind plays a dominant role but there might be other processes influencing the seasonal variability of the CG, such as the interaction with LCEs, nevertheless an in-depth analysis is still needed. In this section, we examine the relationship of the seasonal components of the wind stress curl and the transport through the western arm of the CG, in the presence and in the absence of LCEs. To this end, a zonal section was defined in the CG at 20.2°N and between 96.4°W and 95.6°W (blue line fig. 4b and d), then, the daily transport was computed from the surface to the bottom of the section and annual climatologies were estimated for experiments OBW and NoOBW. The positive transport is defined southward in the section. Figure 7(a) shows these time series along with the annual climatology of the wind stress curl (black line in fig. 7a) averaged over the western BoC (dashed lines in fig. 7b). In both experiments, the climatological transports display a strong seasonality with high values during fall and winter and low values during spring and summer. However, the mean and standard deviation of the transport in OBW (8.5 Sv, σ = 7.1 Sv) are higher than in NoOBW (4.3 Sv, σ = 3.6 Sv), we attribute the difference on the means to the contribution of the deep boundary current to the transport in OBW. As expected, the wind stress curl also displays strong seasonality within the western BoC, with high positive values during fall and winter and low values during spring and summer, obtaining high correlation coefficients between it and the transport in OBW (R=0.81) and NoOBW (R=0.83).

These results are statistically-consistent enough to confirm a major characteristic of the circulation in the BoC, the dominant role of the wind to modulate the seasonal variability of the CG, in agreement with the findings of observational studies like Vázquez de la Cerda et al (2005) and Pérez-Brunius et al (2013). Even though the correlation coefficient between the wind stress curl and transport is slightly higher for OBW, the role of the LCEs is not obvious. The higher standard deviation (σ = 7.1 Sv) and standard error (blue shading fig. 7a) of the transport in OBW suggests that a primary effect of LCEs on the CG circulation is that they impose higher fluctuations in the field. Nevertheless, these fluctuations do not seem to affect the seasonal component of the circulation, but rather the non-seasonal component, this effect is addressed in detail in the following section.

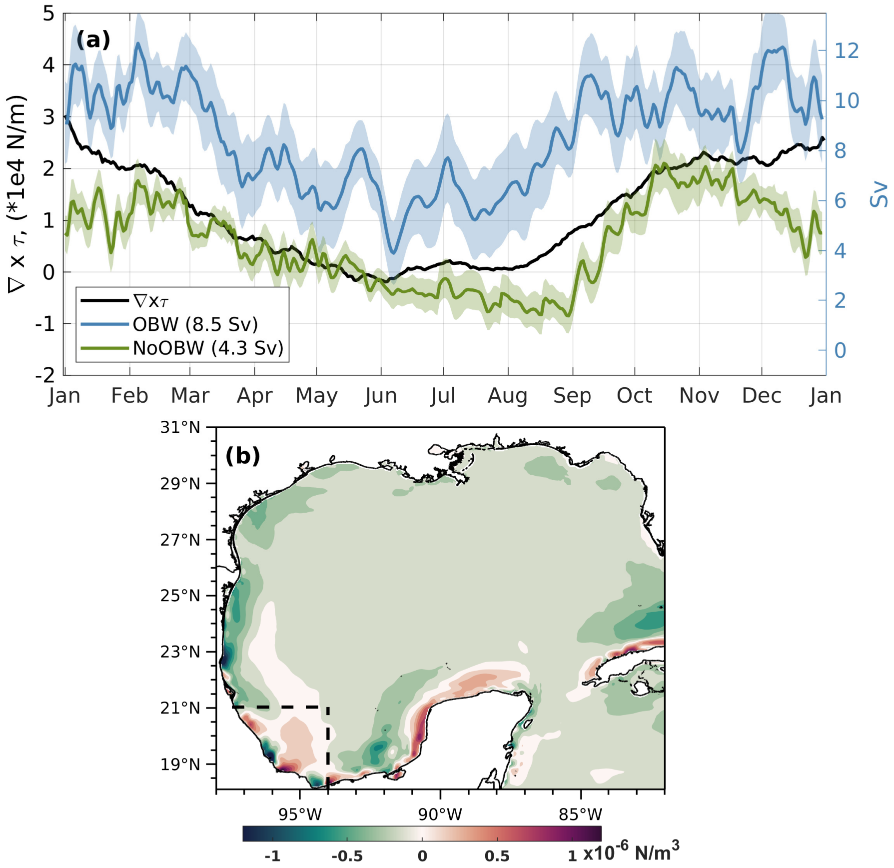

Fig. 7 (a) Annual climatology of the total transport in the CG for experiments OBW and NoOBW and wind stress curl integrated over the BoC, the shading area represents the standard error; and (b) mean wind stress curl over the GoM, the region within the its curl was averaged is indicated with dashed line limits..

3.3 Non-seasonal modulation of the Campeche Gyre

The presence and distribution of the higher fluctuations on the climatological transport in the CG for experiment OBW, compared to NoOBW (Fig. 7a), suggest that LCEs can reach the southwestern boundary of the GoM in virtually any season of the year, contributing to the intraseasonal variability of the BoC circulation. In order to examine in more detail the mechanism by which these fluctuations occur considering a long record of events, we analyzed the trajectories of the 34 LCEs separated from the LC in experiment OBW (figure 2a) and identified 17 LCEs that followed a southern path (Vukovich, 2007) and penetrated into the BoC interacting with the CG. The trajectories of the 17 LCEs are shown in figure 8(a), whose centers are at any given moment in waters deeper than 2000 m. Then, from visual inspection of the surface velocity and SSH fields during these events, time periods when the eddies presented a large southward penetration and whose southern rim influenced the BoC were recorded. Such periods of time are highlighted in orange in the trajectories of figure 8(a), note that most of the events are located south of 23.5°N. To get a representation of the average conditions in the BoC when eddies interact with the CG, a composite of surface velocity vectors and SSH was constructed by computing the mean of these fields over such time periods (Fig. 8b). The composite shows an eddy centered around 95.75°W and 22.5°N with its southern rim reaching 21.5°N, influencing the northern boundary of the BoC. This southward penetration appears to result in a reduction in size and a displacement towards the southwest of the mean CG compared to the normal average conditions (Fig. 4b). However, the weak velocities and lack of closed negative SSH contours in the western basin of the composite can be interpreted as a disruption of the CG from its unperturbed state which, according to the drifter analysis of Pérez-Brunius et al (2013), is given by a loss of mass since part of its waters are displaced and advected away from the BoC by the presence of the LCE.

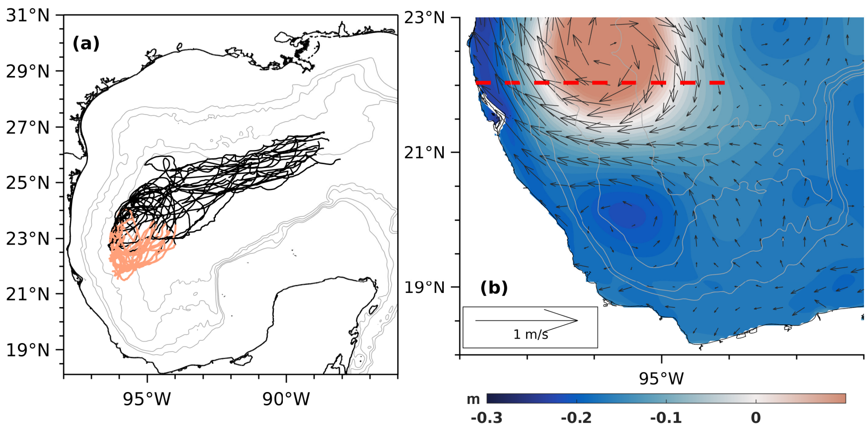

Fig. 8 (a) Trajectories of the 17 LCEs that followed a southern route and passed near the BoC for experiment OBW, time periods when LCEs interacted with the CG are highlighted in orange; and (b) composite of the surface velocity vectors and SSH contours when LCEs interacted with the CG, the red dashed line indicates the zonal section where the vorticity flux computation was done. The gray contours indicate the 500, 1000, 2000, and 3000 m isobaths

Individual events can be addressed by inspecting the daily time series of transport through the entire 19-year simulation. Figure 9(a) (upper panel) shows such time series for experiment OBW with the periods of time when LCEs influenced the BoC highlighted in orange, along with the principal component of the first EOF of the meridional velocity through the zonal section shown in figure 5(g). In addition, a wavelet power spectrum was computed for the corresponding transport (lower panel of figure 9a) following Liu et al (2007), in order see the time scales of variability. The most revealing feature in the figure is that in all the events of LCE southern penetration, the transport through the CG dramatically decreases and, in some "big" events, reverses as shown by the prominent negative peaks, therefore increasing the overall variability. Furthermore, the variability of the principal component is very similar to that of the transport (R=0.79), including the big events. The wavelet analysis shows two prominent peaks of energy: one major peak at around 5 months, distinctly related to the duration of the interplay between the LCEs and the CG, and one minor peak at 12 months, related to the annual signal, which is more energetic in periods with absence of LCEs in the BoC, e.g. years 2011-2012.

To further examine the behavior of the CG, we made a movie which includes the time evolution of the daily SSH and surface velocity vector fields in the BoC, the meridional velocity in the CG zonal section (fig. 4b) and the time series of daily transport through the CG western arm. Such a movie starts in the year 2000 and is included in the online supplemental material. The first big event occurs in 2000, when a LCE starts influencing the northern boundary of the BoC by May, then splits in two and merges again in July. During this period of time and until August, either the LCE or the smaller-in-size eddy after the split-up were fully penetrated in the BoC, replacing the CG and producing weak southward currents in the upper ∼1000m. It is also noticeable from the movie that the reversals in transport sign are associated with times when the northward currents of the western arm of the LCE are located in such a way that they replace the southward currents of the western boundary current of the CG. It is important to note that in periods with absence of LCEs, e.g. from 2008 to 2009 or 2011 to 2012, smaller-in-size anticyclones locally-generated in the BoC also interact with the CG, producing small perturbations in the transport. After reviewing the rest of the events in the movie, it was found that the mechanisms described above operate in all the events of LCE-CG interaction.

Conversely, the transport in experiment NoOBW (fig. 9b) displays a smaller mean (5.1 Sv) and shorter fluctuations with a marked seasonal signal, which is regular throughout the whole period. As in experiment OBW, the variability of the principal component of the first mode is very similar to that of the transport (R=0.73). The wavelet analysis shows a substantial peak of energy at a period of 12 months and a minor peak at 6 months. Finally, the computed daily transport in experiment OBNoW (fig. 9c) shows a low mean and high standard deviation (6.2 Sv, $\sigma = 8$Sv), with a high intraseasonal signal related to the arrival of LCEs in the southwestern GoM. The variability of the principal component of the first mode is very similar to that of the transport (R=0.9).

The global wavelet spectrum shows substantial variability on time scales from 3 months to 2.0 years, with two prominent peaks of energy at periods around 5 and 12 months, clearly related with the presence of LCEs in the BoC.

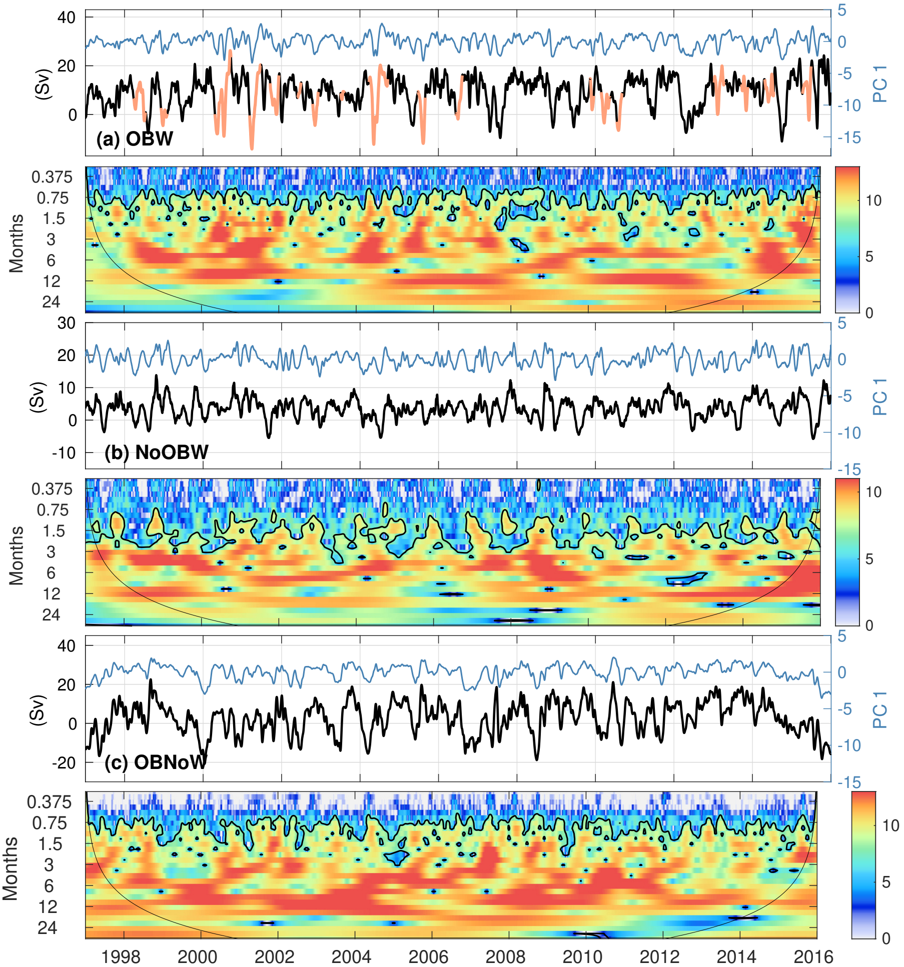

Fig. 9 Time series of daily transport (black lines) through the western boundary current in the CG for experiments (a) OBW, (b) NoOBW and (c) OBNoW and their respective wavelet power spectrum. The regions with greater than 90% confidence are shown with black contours and the "cone of influence", the region where edge effects become important, is also indicated. In (a), time periods when LCEs interact with the CG are highlighted in orange. The principal component of the first EOF mode (blue lines) of the meridional velocity through the zonal section in figure 5 is also shown for the three experiments.

3.3.1 Vorticity flux through the Bay of Campeche

Vorticity plays a central role in geophysical fluid dynamics, with both atmospheric and oceanic large-scale circulations governed by the evolution of potential vorticity. In particular, the Ertel's potential vorticity (PV) is an expression that can be used as a tracer of large-scale ocean circulation since it combines the laws of conservation of mass and angular momentum. Several authors have used the Ertel's PV to study the vorticity flux through different water bodies. From observational data, Beal and Bryden (1999) computed the PV structure across the Agulhas current in order to infer the different origins of the water masses present. The authors found the presence of a "mixing boundary" associated with a sharp upturn in isopycnals, that inhibits cross-stream mixing of intermediate water masses. Candela et al (2002, 2003) and Oey (2004) examined the PV flux between the GoM and the Caribbean Sea using a) time series of current and density measurements across the Yucatan Channel and b) data from a set of global and regional simulations. They found that LCE shedding is preceded by periods of negative vorticity influx into the GoM that causes a retraction of the current, and that influx of positive vorticity tends to extend the Loop Current into the gulf. The examination of the vorticity flux through the BoC provides a way to understand how the vorticity is transferred into or out of the BoC when LCEs interact with the CG, as well as to prove or reject previous hypotheses based on observations.

The simplified Ertel's PV for a stratified fluid is:

$$q \approx -\left[f\frac{\partial \rho}{\partial z} + \frac{\partial v}{\partial x}\frac{\partial \rho}{\partial z} - \frac{\partial v}{\partial z}\frac{\partial \rho}{\partial x} \right] / \rho_0 = q_1 + q_2 + q_3 \quad (3)$$

where (u,v) are the (x,y) components of the velocity and z the vertical coordinate (positive upwards), ρ_0 is a reference mean density, ρ is potential density and f is the Coriolis parameter. The first term on the right-hand side is the planetary vorticity multiplied by the stratification (q_1); the second and third terms represent the horizontal (q_2) and vertical (q_3) shear vorticity including stratification. The the PV flux (PVF) is defined as:

$$PVF = \iint vq dx dz \quad (4)$$

where the double integral is taken over the cross section from the bottom to the surface. The time integral of this flux, called "Cumulative PVF", is:

$$CPVF = \int PVF dt \quad (5)$$

To estimate the PVF through the BoC and examine the behavior of the CG when LCEs collide with the southwestern boundary, we compute the PV terms on equation 3 in a zonal section at 22°N and between 97.6°W and 94.0°W (red dashed line in Fig. 8b) of experiment OBW. The selection of this section was

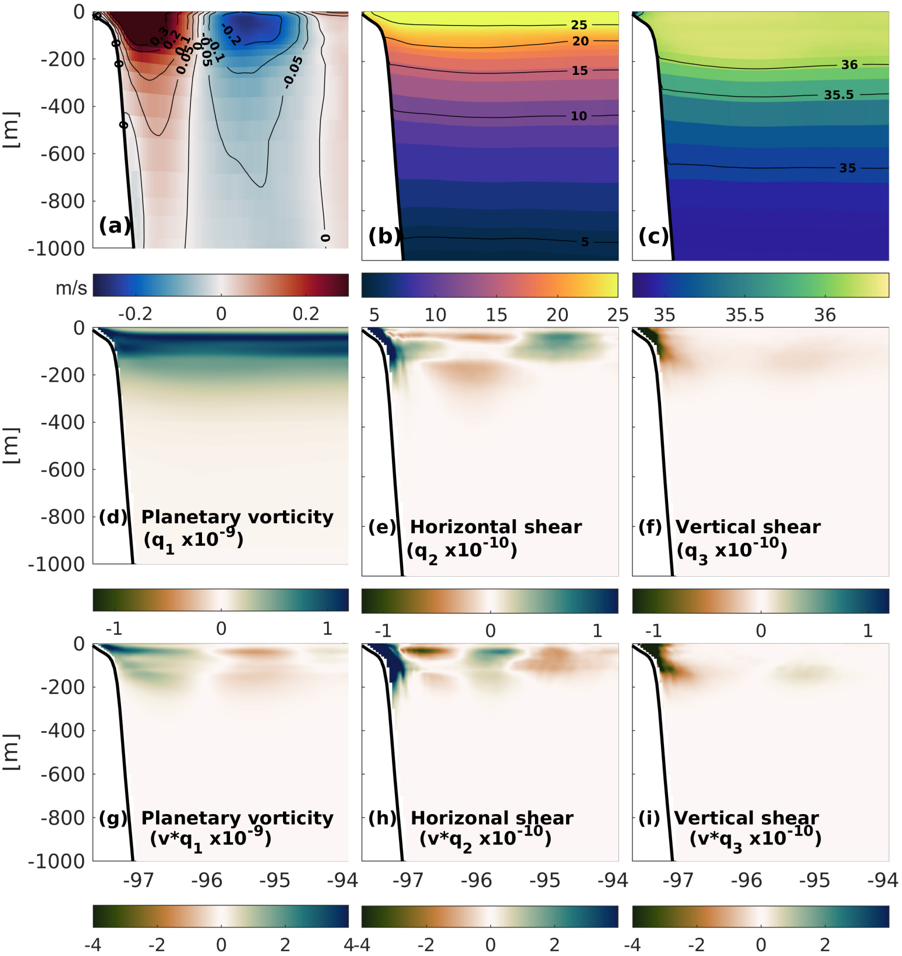

Fig. 10 Mean quantities in a zonal section at 22°N (figure 5b) for experiment OBW: (a) meridional velocity, (b) temperature, (c) salinity, (d) planetary vorticity term q_1 (x10^{-9}), (e) relative vorticity horizontal shear q_2 (x10^{-10}), (f) relative vorticity vertical shear q_3 (x10^{-10}), (g) vq_1 (x10^{-10}), (h) vq_2 (x10^{-11}), and (i) vq_3 (x10^{-11}).

made considering the composite of SSH and surface velocity for periods when LCEs reached this region (Fig. 8b). Figure 10 (a-c) shows the 19-year mean vertical sections of meridional velocity, potential temperature and salinity at 22°N respectively, with a zoom in the upper 1000 m. The v-section shows two high speed current cores, one positive on the western part of the section and one negative to the east, surface-intensified but extending to the bottom with weaker currents, representing a strong anticyclonic circulation on average. Temperature shows strong stratification throughout the section in the upper 1000 m and isothermals near the surface rising and outcropping above the western upper slope. The Salinity contours show the characteristic subsurface salinity maximum at around 100 m represented by the Subtropical Underwater with salinity maximum ≈ 36.50 psu at T ≈ $23C$.

Sections (d-f) in figure 10 show the 19-year means of the three PV terms: q_1, q_2 and q_3. Of the three terms in equation 1, q_1 is the largest although it merely reflects the strong stratification near the surface. The q_2 depicts a region of strong positive shear near the surface on the western part of the section, that could be related to the interaction of LCEs with the continental slope, and a secondary area of negative shear to the east, related to the center of the mean anticyclonic circulation in figure 10a. The q_3 is also largest near the surface on the western portion of the channel, but has small magnitudes in comparison to q_2. In addition, mean sections of "vq" reflect the q values weighted by v (Fig. 10 g-i). The mean vq_1 and vq_3 show large magnitudes near the surface but with opposite patterns and with vq_1 an order of magnitude larger. The mean vq_2 shows large magnitude on the western side of the channel, in the northward current core of the mean eddy. It will become evident that most of the contribution to PV F2 is from those vq_2-values.

On the other hand, the PVF due to q_1 is largest, but we found that it is unrelated to the LCEs variability in the southwestern GoM; PVF due to q_3 is highly anti-correlated with the PVF due to q_2 but smaller. Therefore, we only discuss the vorticity flux associated with the horizontal shear (PVF2), which is the component closely related with the presence of LCEs in the southwestern GoM. Figure 11 shows the time series of PVF2(a) and CPFV2(b) along with the integrated relative vorticity within the BoC. PVF2 has been low-passed to remove signals shorter than 15 days, and CPFV2 has been detrended (following Candela et al (2002, 2003)), which allow us to get a better view of the crests and troughs of the generally monotonic function CPFV2. In both cases, time periods when LCEs penetrated into the BoC are highlighted in orange. The most revealing characteristic is that in each of the 17 events, the presence of LCEs coincide with the peaks in the PVF2 curve, indicating a northward flux of positive vorticity from the BoC, which is higher in some events than others. In fact, the most prominent peaks in the time series occur during LCE penetration events. Using the same reasoning as Candela et al (2002, 2003) and Oey (2004), this can be interpreted as a flux of fluid parcels with strengthening cyclonic vorticity out of the BoC. In either case, it explains the deceleration/interruption of the CG inferred in the previous section during these events, where a decrease of the integrated relative vorticity within the BoC is also observed (gray line fig. 11a). We also see that PVF2 is entirely positive, a consequence of the dominant cyclonic shears on the western portion of the section (continental slope) near the surface, and the strong northward velocities there; and that in the absence of LCEs, PVF2 is weaker.

The behavior of CPVF2 (Fig. 11b), which is characterized by alternating periods of positive and negative fluxes lasting several months, is evident in the presence of LCEs. Over the 19-year simulation, virtually all the periods when LCEs penetrated into the BoC occurred during a period of cyclonic flux, or upward "trend", of CPVF2 out of the BoC, which in some cases are more extended than others (e.g. years 2000 and 2004). These results suggest that the northward flux of positive vorticity is driven by the strong positive shears weighted by the northward velocities of the western branch of a LCE penetrating in the BoC. This also supports the results found by Pérez-Brunius et al (2013) in which the presence of LCEs against the northwestern boundary of the BoC disrupted the cyclonic gyre, rather than intensify it by means of influx of positive vorticity into the BOC by cyclones generated in LCE collisions, as originally proposed by Vidal et al (1992).

To provide further insight into the influence of LCEs on the CG circulation, we incorporated the time evolution of the meridional velocity in the 22°N zonal section, the vq sections at 22°N and the time series of PVF2 and CPFV2 in the movie of the supplemental material. From figure 11, it is observed that years 2000 and 2004 present LCE penetration events where PV flux is the highest. Indeed, in both events it is observed that the peaks in PVF2 are related to strong southward penetration of the LCEs into the BoC. This produces strong velocity shears in the western portion of the section which in turn are correlated with reversals in the circulation of the CG.

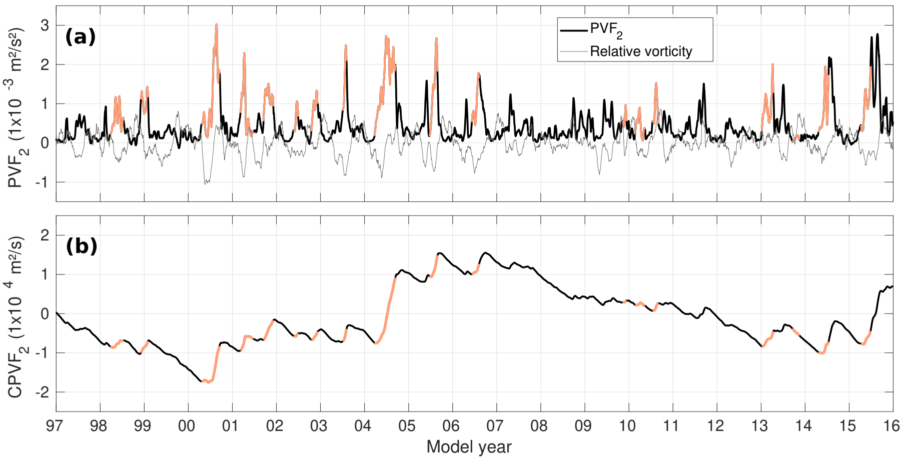

Fig. 11 (a) Time series of horizontal shear flux (integrated vq2) through the zonal section at 22°N; and (b) cumulative horizontal shear flux through 22°N. Time periods when LCEs interacted with the CG are highlighted in orange. In (a), relative vorticity integrated over the BoC (gray line) is also shown.

4 Summary and conclusions

In this study, we addressed the role that the wind and LCEs play in the mean, seasonal and non-seasonal modulation of the CG, by performing a set of long-term free-running numerical simulations of a GoM configuration using HYCOM, in which we turn on and off these two forcings. The multiannual nature of these experiments provided confidence about the statistical consistency of our results, since they were able to capture the regular (year by year) contribution of wind to the BoC circulation and represent a long record of events when LCEs interacted with the CG. According to experiment NoOBW, in the absence of LCEs, the wind is able to sustain a surface-intensified, symmetric cyclonic circulation in the western BoC, confined within the upper ∼600 m. When the LC system is taken into consideration in experiment OBW, and therefore the events when LCEs influence the BoC, a cyclonic circulation is also present below ∼1000 m, with mean velocities of ∼5 cm/s throughout the water column, resulting in the CG apparently extending to the bottom. Nevertheless, our results indicate that this feature is merely the expression of the larger-scale cyclonic bottom boundary current (Pérez-Brunius et al, 2018; Morey et al, 2020). According to OBNoW, in the absence of wind, a mean eddy-driven, equivalent-barotropic cyclonic circulation in the upper layers of the western BoC is present (Fig. 11c). The diagnostic of vertical coherence confirmed that equivalent-barotropic flows can develop in a similar way under these different dynamic conditions, corroborating the importance of the topography in organizing upper layer flows.

The high correlation coefficients (R≈0.8) between the climatological transport in the western arm of the CG for OBW and NoOBW, and the seasonal component of the wind stress curl averaged over the BoC, provided evidence about the seasonal modulation of the BoC. We have learned that one primary effect of LCEs is to impose high fluctuations on the transport of the CG, contributing to its intraseasonal variability. When the interaction with LCEs is strong, these fluctuations lead to reversals in the transport which occur when the northward currents of the western arm of the LCE replace the southward currents of the western arm of the CG. This results in the interruption of the CG from its unperturbed state more than an intensification, as had been originally proposed and hypothesized in previous studies (Vidal et al, 1992; Vázquez de la Cerda et al, 2005). We found that the vorticity flux due to horizontal shear through the BoC can be used as an indicator of the interaction of LCEs with the CG. The model results indicate that a northward flux of cyclonic vorticity out of the BoC, which is also related with a decrease in relative vorticity within the region, occurs during periods of LCE southern penetration, resulting in the disruption of the CG. These mechanisms are found to be consistent in all the events throughout the entire simulation.

Our results indicate that the wind stress curl and LCEs are the primary forcings influencing the CG variability, and that topography controls the location and extention of the gyre. However, additional approaches to deepen on the role of this factor can be explored: one such alternative is to perform artificial modifications of the bathymetry over the BoC in such a way that potential vorticity contours f/F_0 are open instead of closed, in order to avoid the development of an equivalent barotropic flow and estimate the impact. Such an analysis is proposed for future research. Although we identified some events in the three experiments, especially for OBW, further studies are needed to establish the mechanisms and contribution of locally-generated eddies to the variability in the BoC.

Supplementary information. This version of the article includes a movie as a supplementary material archived in the Zenodo repository https://doi.org/10.5281/zenodo.6505406

Acknowledgments. The first author thanks the program of postdoctoral fellowships UNAM-DGAPA, as well as the Instituto de Ciencias de la Atmósfera y Cambio Climático of the Universidad Nacional Autónoma de México for the use of the cluster Ometeotl to run the simulations. The authors thank the support of Pavel Oropeza in setting up the HPC environment for the execution of the simulations, and Susana Higuera and Juan Nieblas for their help in processing the data for the validation of the model. We thank the editor, Dr. Ricardo de Camargo and the two anonymous reviewers for valuable contributions to the manuscript. Erick R. Olvera-Prado would like to thank Eric Chassignet, Steve Morey and Alex Bozec (Florida State University) for their advice, motivation and guidance in conducting an equivalent set of simulations during his PhD studies.

Declarations

- **Funding** This study was funded by the program of postdoctoral fellowships UNAM DGAPA
- **Conflict of interest** The authors declare no competing interests.
- **Data availability** The datasets generated during and/or analyzed during the current study are not publicly available but may be available from the corresponding author on reasonable request.

References

Athié G, Sheinbaum J, Leben R, et al (2015) Interannual variability in the yucatan channel flow. Geophysical Research Letters 42(5):1496–1503. https://doi.org/10.1002/2014GL062674

Athie G, Sheinbaum J, Candela J, et al (2020) Seasonal variability of the transport through the yucatan channel from observations. Journal of Physical Oceanography 50:343–360

Beal LM, Bryden HL (1999) The velocity and vorticity structure of the agulhas current at 32°s. Journal of Geophysical Research: Oceans 104(C3):5151–5176. https://doi.org/10.1029/1998JC900056

Bleck R (2002) An oceanic general circulation model framed in hybrid isopycnic-cartesian coordinates. Ocean Modelling 4(1):55–88

Candela J, Sheinbaum J, Ochoa J, et al (2002) The potential vorticity flux through the yucatan channel and the loop current in the gulf of mexico. Geophysical Research Letters 29(22):16–1–16–4. https://doi.org/10.1029/2002GL015587

Candela J, Tanahara S, Crepon M, et al (2003) Yucatan channel flow: Observations versus clipper atl6 and mercator pam models. Journal of Geophysical Research: Oceans 108(C12):15–1–15–24. https://doi.org/https://doi.org/10.1029/2003JC001961

Candela J, Ochoa-de-la Torre J, Sheinbaum J, et al (2019) The flow through the gulf of mexico. Journal of Physical Oceanography https://doi.org/10.1175/JPO-D-18-0189.1

Vázquez de la Cerda AM, Reid RO, DiMarco SF, et al (2005) Bay of campeche circulation: An update. In: Sturges W, Lugo-Fernandez A (eds) Circulation in the Gulf of Mexico: Observations and Models. American Geophysical Union (AGU), p 279–293, https://doi.org/10.1029/161GM20

Chassignet EP, Hurlburt HE, Smedstad OM, et al (2006) Generalized vertical coordinates for eddy-resolving global and coastal ocean forecasts. Oceanography 19

Dimarco S, Jr N, Reid R (2005) A statistical description of the velocity fields from upper ocean drifters in the gulf of mexico. Washington DC American Geophysical Union Geophysical Monograph Series 161:101–110. https://doi.org/10.1029/161GM08

Donohue KA, Hamilton P, Leben R, et al (2008) Survey of deepwater currents in the northwestern gulf of mexico, volume 2: Technical report. MMS Tech. Rep. MMS 2008-031, MMS

Dukhovskoy DS, Leben RR, Chassignet EP, et al (2015) Characterization of the uncertainty of loop current metrics using a multidecadal numerical simulation and altimeter observations. Deep-Sea Research Part I 100:140–158. https://doi.org/10.1016/j.dsr.2015.01.005

Furey H, Bower A, Perez-Brunius P, et al (2018) Deep Eddies in the Gulf of Mexico Observed with Floats. Journal of Physical Oceanography 48(11):2703–2719. https://doi.org/10.1175/JPO-D-17-0245.1

Leben RR (2005) Altimeter-derived loop current metrics. In: Sturges W, Lugo-Fernandez A (eds) Circulation in the Gulf of Mexico: Observations and Models. American Geophysical Union (AGU), p 181–201

Liu Y, San Liang X, Weisberg RH (2007) Rectification of the Bias in the Wavelet Power Spectrum. Journal of Atmospheric and Oceanic Technology

24(12):2093–2102. https://doi.org/10.1175/2007JTECHO511.1

Metzger E, Helber R, Hogan P, et al (2017) Global ocean forecast system 3.1 validation testing p 60

Monreal-Gómez MA, Salas de León D (1997) Circulación y estructura termohalina del golfo de méxico. Contribución a la Oceanografía Física en México, Monogr Unión Geofís Mex 3:1045–1064

Morey SL, Gopalakrishnan G, Pallás Sanz E, et al (2020) Assessment of numerical simulations of deep circulation and variability in the gulf of mexico using recent observations. Journal of Physical Oceanography 50:1045–1064. https://doi.org/10.1175/JPO-D-19-0137.1

Oey LY (2004) Vorticity flux through the yucatan channel and loop current variability in the gulf of mexico. Journal of Geophysical Research 109. https://doi.org/10.1029/2004JC002400

Ohlmann JC, Niiler PP, Fox CA, et al (2001) Eddy energy and shelf interactions in the gulf of mexico. Journal of Geophysical Research: Oceans 106(C2):2605–2620. https://doi.org/10.1029/1999JC000162

Olvera-Prado ER, Moreles E, Zavala-Hidalgo J, et al (2022) Upper-lower layer coupling of recurrent circulation patterns in the gulf of mexico. Journal of Physical Oceanography https://doi.org/10.1175/JPO-D-21-0281.1

Pérez-Brunius P, García-Carrillo P, Dubranna J, et al (2013) Direct observations of the upper layer circulation in the southern gulf of mexico. Deep Sea Research Part II: Topical Studies in Oceanography 85:182 – 194. https://doi.org/10.1016/j.dsr2.2012.07.020, modern Physical Oceanography and Professor H.T. Rossby

Pérez-Brunius P, Furey H, Bower A, et al (2018) Dominant circulation patterns of the deep gulf of mexico. Journal of Physical Oceanography 48(3):511–529. https://doi.org/10.1175/JPO-D-17-0140.1

Romanou A, Chassignet EP, Sturges W (2004) Gulf of mexico circulation within a high-resolution numerical simulation of the north atlantic ocean. Journal of Geophysical Research: Oceans 109(C1). https://doi.org/10.1029/2003JC001770

Rousset C, Beal LM (2010) Observations of the florida and yucatan currents from a caribbean cruise ship. Journal of Physical Oceanography 40(7):1575–1581. https://doi.org/10.1175/2010JPO4447.1

Saha S, Moorthi S, Pan HL, et al (2010) The ncep climate forecast system reanalysis. Bulletin of the American Meteorological Society 91(8):1015–1058.

https://doi.org/10.1175/2010BAMS3001.1

Sheinbaum J, Candela J, Badan A, et al (2002) Flow structure and transport in the yucatan channel. Geophysical Research Letters 29(3):10–1–10–4. https://doi.org/10.1029/2001GL013990

Gutiérrez de Velasco G, Winant CD (1996) Seasonal patterns of wind stress and wind stress curl over the gulf of mexico. Journal of Geophysical Research: Oceans 101(C8):18,127–18,140. https://doi.org/10.1029/96JC01442

Vidal VMV, Vidal FV, Pérez-Molero JM (1992) Collision of a loop current anticyclonic ring against the continental shelf slope of the western gulf of mexico. Journal of Geophysical Research: Oceans 97(C2):2155–2172. https://doi.org/10.1029/91JC00486

Vukovich FM (2007) Climatology of ocean features in the gulf of mexico using satellite remote sensing data. Journal of Physical Oceanography 37(3):689–707. https://doi.org/10.1175/JPO2989.1

Zavala-Hidalgo J, Morey SL, O'Brien JJ (2003) Seasonal circulation on the western shelf of the gulf of mexico using a high resolution numerical model. Journal of Geophysical Research: Oceans (1978–2012) 108(C12). https://doi.org/10.1029/2003JC001879

Zavala Sansón L (2019) Nonlinear and time-dependent equivalent-barotropic flows. Journal of Fluid Mechanics 871:925–951. https://doi.org/10.1017/jfm.2019.354